Computer Methods in Applied Mechanics and Engineering 448 (2026) 118454

Contents lists available at ScienceDirect

Computer Methods in Applied Mechanics and Engineering

journal homepage: www.elsevier.com/locate/cma

Aerodynamics-driven topology optimization of compliant airfoils considering stability

Qingdi Wang [a], Lucas Oliveira Siqueira [b], Tao Xu [a], Guanzhe Cui [c], Zhi Li [a], Anderson Soares da Costa Azevêdo [b], Renato Picelli [b], Yi Min Xie [a,d,*]

[a] Centre for Innovative Structures and Materials, School of Engineering, RMIT University, Melbourne, Victoria 3000, Australia
[b] Polytechnic School, University of São Paulo, São Paulo 05508-030, Brazil
[c] Department of Mechanical Engineering, School of Engineering, The University of Melbourne, Parkville, Victoria 3010, Australia
[d] College of Future Technologies, Hohai University, Changzhou, Jiangsu 213200, China

ARTICLE INFO

Keywords:
Topology optimization
Aerodynamics
Wing ribs
Fluid–structure interaction
Structural stability
Buckling

ABSTRACT

Airfoil structures optimized solely for stiffness can suffer from buckling instabilities under realistic aerodynamic loads. We present the first topology optimization framework to improve the stability of aerodynamic structures. For a clear representation of structure, this work employs the topology optimization of binary structures with geometry trimming. Reynolds-averaged Navier-Stokes turbulence model is employed to accurately predict the turbulent aerodynamic loading under realistic flight conditions. Fluid–structure interaction and buckling analysis are conducted using an elastic formulation with geometrical nonlinearities to allow for large deformations. The numerical model system is solved through the finite element method and the Arbitrary Lagrangian-Eulerian method is applied. The sensitivities are calculated using semi-automatic differentiation and interpolated to the optimization mesh. Kreisselmeier-Steinhauser aggregation function is used and augmented Lagrangian multipliers are developed for buckling constraints. Numerical examples demonstrate that the proposed method can effectively improve the airfoil stability to different constraint levels across various configurations with minimal parameter tuning. Additionally, the algorithm produces designs that are conducive to manufacturing.

1. Introduction

The wing of an aircraft is an airfoil section that generates lift during takeoff and landing. Aircraft wings play a crucial role in providing flight characteristics such as control, lift, balance, and stability. The construction of a wing typically involves structural components including skin, ribs, stringers, and spars. Among these, the wing rib is particularly important as it maintains the airfoil shape without large distortion, and transfers loads from the skin to the other components [1] (Fig. 1).

Topology optimization represents a revolution from conventional sizing methods because it achieves significant weight savings by optimizing material distribution while maintaining structural integrity [2]. It has been applied on aircraft structures for nearly three decades [3]. Most airfoil optimization work has the objective of improving its aerodynamic characteristics at multiple operating points, while the internal structure topology optimization has not been extensively studied [4–15]. Several studies have optimized the aircraft wing ribs or airfoils. For example, Krog et al [16] used an energy-based topology optimization approach to optimize Airbus A380 wing

* Corresponding author.
E-mail address: mike.xie@rmit.edu.au (Y.M. Xie).

https://doi.org/10.1016/j.cma.2025.118454
Received 30 May 2025; Received in revised form 30 September 2025; Accepted 2 October 2025

box ribs under multiple local loads, and Elelwi et al [2] applied Solid Isotropic Material with the Penalization (SIMP) optimization to reduce weight for fixed and moving wing segments driven by computational fluid dynamics (CFD) pressures. Proenca et al [17] and Walker & Liu [18] generated truss-like interiors for NACA 0012 and NACA 23015 airfoils via SIMP. Aage et al [19] then used giga-voxel-resolution computational morphogenesis to generate highly detailed internal wing structures. More recently, Gomes & Palacios [20] developed a strategy for density-based topology optimization of fluid–structure interaction (FSI) of compliant airfoil. Kambayashi et al [21] developed aerodynamic-driven topology optimization of compliant morphing airfoils using a panel method. Despite the fact that those studies maximized the structural stiffness, the slender members generated inside wings through topology optimization are under compression, and they are characteristically vulnerable to buckling. The recent study has also reported the occurrence of unstable airfoil structure that buckles under the FSI loads in topology optimization [20]. Currently, the existing studies only focus on stiffness maximization, and the structural stability has not yet been considered into the optimization so far.

Structural instability (buckling) can occur on slender structures under compression, such as wing skin or wing ribs. Compressive stresses in compliant aerospace component can drive such failure before material yielding. Currently, researchers need to perform buckling analysis on ribs of wings in multiple shapes in order to find the best design for buckling strength [22]. There is a lack of studies to optimize aerodynamic structure stability. In this work, we propose a framework of improving the wing ribs or airfoil stability using topology optimization with FSI.

Discrete topology optimization methods are widely used in FSI applications because they yield clear solid-void layouts. In contrast, density based approaches produce intermediate (“gray”) elements that not only demand heuristic post-processing but can also introduce pseudo buckling modes [23]. In this work, we use discrete topology optimization method with binary design variables to inherently eliminate those artifacts and directly satisfy the consideration of manufacturing requirements [24].

In this study, we propose an extended binary topology optimization framework on a compliant airfoil, with the aim of enhancing its structural stability under aerodynamic load. Unlike all prior topology optimization research where the focus is only stiffness, this research considers the buckling in the optimization approach. To the best of our knowledge, this is the first topology optimization study of an airfoil considering stability. Also, this work emphasizes aerodynamic factors which requires the use of high-fidelity fluid modeling with turbulent model. Additionally, given the highly nonlinear nature of aerodynamic and buckling problems, this approach considers large displacement and geometric non-linearity in FSI and buckling analyses.

The computational tool used is COMSOL Multiphysics which has been verified for a range of aeronautical applications, e.g. in Malikov et al [25]. Detailed explanations of the FSI and buckling analysis methods are introduced in Section 2, which is followed by the optimization method in Section 3. Section 4 contains computational procedures and Section 5 presents the numerical results from the proposed method.

2. Formulation

The mathematical and physical framework that we used are introduced in this section. In this work, the FSI and buckling analysis are employed. The fluid flow is considered to be turbulent. In order to resolve the small scale of turbulent fluid flow, the Reynolds-Averaged Navier-Stokes (RANS) equations method is used. Moving mesh is employed for the fluid structural interface and structural nonlinear responses are evaluated in the solid domain.

2.1. Fluid–structure interaction

The airfoil computational domain consists of fluid domain Ω_f and solid domain Ω_s. These two domains do not overlap and are separated by the fluid–solid interface Γ_{fs}. Throughout this paper, fluid–structure interaction represents a two-way, partitioned, strongly coupled procedure: interface displacements are fed back to the fluid, fluid tractions are applied to the solid, and the fluid and structural subproblems are iterated until equilibrium is achieved.

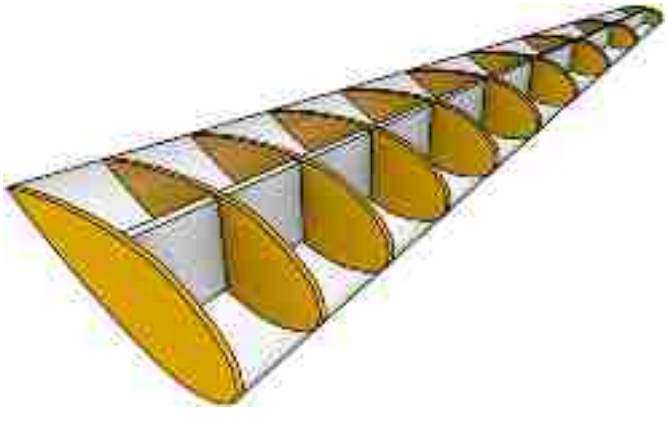

Fig. 1. A typical structural arrangement of a wing showing the skin, ribs (in yellow) and main spar.

2.1.1. Fluid dynamics

In the fluid domain Ω_f, the incompressible isothermal viscous fluid flow is employed. The fluid flow without body force is described by continuity and Navier-Stokes equations. The continuity equation associated with fluid velocity vector $\mathbf{v}$ is

$$\nabla \cdot \mathbf{v} = 0 \quad \text{in}\Omega_f \tag{1}$$

In an Eulerian (spatial) framework, considering turbulent flow computations, the RANS form of the momentum equation is expressed as

$$\rho_f(\mathbf{v}\cdot\nabla)\mathbf{v} = -\nabla p + \nabla\cdot\left[\mu_f\left(\nabla\mathbf{v} + (\nabla\mathbf{v})^T\right)\right] + \nabla\cdot\boldsymbol{\tau}_R \quad \text{in}\Omega_f \tag{2}$$

where the fluid density is ρ_f and dynamic viscosity is μ_f. Fluid pressure is denoted by p. $\boldsymbol{\tau}_R$ is the Reynolds stress tensor, from the Boussinesq approximation, expressed as

$$\boldsymbol{\tau}_R \approx 2\mu_t\mathbf{S} - \frac{2}{3}\rho_f k\mathbf{I}, \qquad \mathbf{S} = \frac{1}{2}\left(\nabla\mathbf{v} + (\nabla\mathbf{v})^T\right) \tag{3}$$

where μ_t is the turbulent or eddy viscosity, k is the turbulent kinetic energy and $\mathbf{I}$ is the unit diagonal matrix.

To model the external aerodynamic flow, we employ the standard RANS k-ε model, which is widely validated, robust, and computationally efficient for external flow simulations. Its formulation introduces two additional transport equations for turbulent kinetic energy k and its dissipation rate ε. The kinetic energy k equation is:

$$\rho_f\mathbf{v}\cdot\nabla k = \nabla\cdot\left[\left(\mu_f + \frac{\mu_t}{\sigma_k}\right)\nabla k\right] + P_k - \rho_f\varepsilon \tag{4}$$

where P_k is the production term expressed as:

$$P_k = \mu_t\left[\nabla\mathbf{v} : \left(\nabla\mathbf{v} + (\nabla\mathbf{v})^T\right)\right] \tag{5}$$

The dissipation rate equation is:

$$\rho_f\mathbf{v}\cdot\nabla\varepsilon = \nabla\cdot\left[\left(\mu_f + \frac{\mu_t}{\sigma_\varepsilon}\right)\nabla\varepsilon\right] + C_{\varepsilon 1}\frac{\varepsilon}{k}P_k - C_{\varepsilon 2}\rho_f\frac{\varepsilon^2}{k} \tag{6}$$

where the turbulent viscosity μ_t is calculated by:

$$\mu_t = C_\mu\rho_f\frac{k^2}{\varepsilon} \tag{7}$$

Thise set of equations includes five constants, and standard values are used in this study:

$$C_\mu = 0.09, \quad \sigma_k = 1.44, \quad \sigma_\varepsilon = 1.92, \quad C_{\varepsilon 1} = 1.0, \quad C_{\varepsilon 2} = 1.3 \tag{8}$$

2.1.2. Structural domain model

The aerodynamic structure is described using the Total Lagrangian approach, capable of capturing large displacement nonlinear effects [26]. The structural domain Ω_s is modeled in a Lagrangian reference frame. All finite element equations are derived with respect to the initial (undeformed) configuration of the structure. In this setting, the displacement vector $\mathbf{u}$ accounts for the displacement from each initial (material) coordinates $\mathbf{X}$ to its deformed spatial position $\mathbf{x}$. Consequently,

$$\mathbf{x} = \mathbf{X} + \mathbf{u} \tag{9}$$

Then deformation gradient tensor $\mathbf{F}$ is introduced below,

$$\mathbf{F} = \nabla_{\mathbf{X}}\mathbf{x} = \mathbf{I} + \nabla_{\mathbf{X}}\mathbf{u} \tag{10}$$

where $\nabla_{\mathbf{X}}\mathbf{u}$ denotes the displacement gradient tensor, given by the derivatives of the deformed coordinates with respect to the original coordinates. The strain in the reference (material) configuration is measured with the Green-Lagrange strain tensor, expressed as

$$\mathbf{E} = \frac{1}{2}\left(\mathbf{F}^T\mathbf{F} - \mathbf{I}\right) \tag{11}$$

where $\mathbf{F}^T\mathbf{F}$ is known as the right Cauchy-Green deformation tensor. Both $\mathbf{E}$ and $\mathbf{F}^T\mathbf{F}$ exclude any rigid-body strains. Under static equilibrium, the balance equation is described in terms of the second Piola-Kirchhoff stress tensor $\mathbf{S}$:

$$\nabla_{\mathbf{X}}\cdot(\mathbf{FS}) = \mathbf{0} \tag{12}$$

The weak form (via the principle of virtual work):

$$\int_{\Omega_s} \delta\mathbf{E} : \mathbf{S} d\Omega = \int_{\Gamma_{fs}} \delta\mathbf{u} \cdot \mathbf{t}_s d\Gamma \tag{13}$$

where $\mathbf{t}_s$ is the external force applied at the fluid–structural interface.

The linear constitutive relation between the strain tensor $\mathbf{E}$ and the stress tensor $\mathbf{S}$ can be described by employing the Saint Venant-Kirchhoff model, which is expressed by

$$\mathbf{S} = \lambda_s \mathrm{tr}(\mathbf{E})\mathbf{I} + 2\mu_s \mathbf{E} \tag{14}$$

where Lamé constants λ_s and shear modulus μ_s are derived from Young's modulus E and Poisson's ratio ν:

$$\lambda_s = \frac{E\nu}{(1+\nu)(1-2\nu)}, \quad \mu_s = \frac{E}{2(1+\nu)} \tag{15}$$

2.1.3. Arbitrary lagrangian–Eulerian (ALE) mesh movement and coupling

To capture the effect of large structural deformations on the fluid domain boundaries in the FSI, the Arbitrary Lagrangian–Eulerian (ALE) method is used to update the fluid mesh. Letting d denote fluid mesh displacement, linear elasticity-like equation is satisfied within fluid domain Ω_f:

$$\nabla \cdot (\mathbf{K}_m \nabla \mathbf{d}) = \mathbf{0} \quad \text{in}\Omega_f \tag{16}$$

where $\mathbf{K}_\mathrm{m}$ is mesh stiffness tensor.

For fluid–structure interface coupling condition, both kinematic continuity and dynamic equilibrium are guaranteed. To achieve kinematic balance in this steady-state analysis, fluid mesh displacement matches the structural displacement at the fluid–structure interface Γ_{fs}:

$$\mathbf{d} = \mathbf{u} \quad \text{on}\Gamma_{fs} \tag{17}$$

Once the mesh is updated, the flow is solved on this deformed mesh.

Structural deformations are fed back to the aerodynamic mesh via ALE mesh motion, the fluid tractions are returned to the solid, and the flow and structure are iterated to convergence. For equilibrium of forces at the interface, the traction from the fluid must balance the traction on the structure:

$$\mathbf{t}_f + \mathbf{t}_s = \mathbf{0} \quad \text{on}\Gamma_f \tag{18}$$

where the interface forces applied by the fluid and solid are defined as:

$$\mathbf{t}_f = \boldsymbol{\sigma}_f \cdot \mathbf{n}_f, \qquad \mathbf{t}_s = \boldsymbol{\sigma}_s \cdot \mathbf{n}_s \tag{19}$$

and noting that the unit normal vectors pointing outward from the solid and fluid domain at the fluid–structure interface $\mathbf{n}_s = \mathbf{n}_f$. In Eq. (19), $\boldsymbol{\sigma}_s$ is the structural Cauchy stress and $\boldsymbol{\sigma}_f$ is the fluid Cauchy stress tensor shown as below.

$$\boldsymbol{\sigma}_f = -p\mathbf{I} + \mu\left(\nabla \mathbf{u}_f + \left(\nabla \mathbf{u}_f\right)^T\right) + \boldsymbol{\tau}_R \tag{20}$$

2.2. Buckling analysis

After solving the FSI step in Section 2.1.2, the converged pre-stressed displacement is represented by $\mathbf{u}_0$. Based on the Equations, the geometrically nonlinear equilibrium ready for considering stability or buckling is:

$$\nabla_\mathbf{X} \cdot \mathbf{P}(\mathbf{u}_0) = \mathbf{0} \quad \text{in}\Omega_s \tag{21}$$

where $\mathbf{P} = \mathbf{FS}$ is the first Piola-Kirchhoff stress. The equilibrium's weak form (virtual-work statement) is:

$$\int_{\Omega_s} \delta\mathbf{E} : \mathbf{S}(\mathbf{u}_0) d\Omega = \int_{\Gamma_{fs}} \delta\mathbf{u} \cdot \mathbf{t}_s d\Gamma \tag{22}$$

The stability of the deformed (pre-stressed) structure is determined using an eigenvalue problem as follows:

$$[\mathbf{K}_T(\mathbf{u}_0) + \lambda \mathbf{K}_\sigma(\mathbf{u}_0)]\boldsymbol{\phi} = \mathbf{0} \tag{23}$$

where $\mathbf{K}_\sigma(\mathbf{u}_0)$ denotes the geometric (stress) stiffness matrix accounting for stress stiffening effects and it is assembled from Gauss-point stresses in each element. λ is the scalar eigenvalue and it is commonly called the load multiplier or buckling factor, representing the factor at which the load leads to buckling. $\boldsymbol{\phi}$ represents buckling mode shape associated with λ. The tangent stiffness matrix $\mathbf{K}_\mathrm{T}$ at the displacement $\mathbf{u}_0$ is defined using the formula below:

$$\mathbf{K}_T(\mathbf{u}_0) = \mathbf{K}_{\mathrm{mat}}(\mathbf{u}_0) + \mathbf{K}_{\mathrm{geom}}(\mathbf{u}_0) \tag{24}$$

where $\mathbf{K}_T$ includes both material stiffness $\mathbf{K}_{mat}$ and geometric stiffness $\mathbf{K}_{geom}$ due to the stress state from the FSI load. This matrix is used for analyzing how the structure reacts with geometric nonlinearity.

In Eq. (23) representing the linearized eigenvalue buckling analysis with geometric nonlinearity, each solved eigenpair (λ_i, $\boldsymbol{\varphi}_i$) represents the ith-order buckling load factor and its associated mode shape. In most structural applications only the lowest few modes govern stability, so we compute the first q modes. In our case $q = 12$, and we focus on the first mode λ_1 which dictates the onset of buckling in engineering designs.

In our analysis, any negative buckling factors are not calculated, because they correspond to loading scenarios in the opposite direction that fall outside the real aerodynamic application [27]. We then sort all positive eigenvalues in ascending order and identify the smallest as the critical buckling factor (λ_{crit}) from Eq. (23). The solved multiplier λ_1 from Eq. (23) reflects the smallest value at which the external fluid loading will cause the structure to buckle. It indicates that if the original FSI load is scaled or multiplied by λ_1, the structure hits the instability point.

$$\lambda_{crit} = \lambda_1 \tag{25}$$

2.3. Simulation workflow (flow-structure-buckling)

For a given binary design, the analysis is conducted as a workflow that uses the fluid and solid governing equations in Section 2.1 and 2.2.

1. Start from initial fluid velocity $\mathbf{v}$, pressure p and solid displacement fields $\mathbf{u}$ (from the previous iterate).
2. With the current interface displacement and velocity, solve the incompressible RANS equations on the current fluid domain to obtain $\mathbf{v}$, p and fluid Cauchy stress $\boldsymbol{\sigma}_f$
3. Compute fluid tractions $\mathbf{t}_f$ on the interface Γ_{fs}.
4. Apply $\mathbf{t}_f$ to the solid and solve the total Lagrangian equilibrium for the updated displacement $\mathbf{u}$, strains and solid stress $\boldsymbol{\sigma}_s$
5. Apply kinematic and traction continuity equations on the interface Γ_{fs}: displacement match, and equal and opposite tractions from solid and fluid.
6. Check that fluid and solid residuals and the interface mismatch fall below prescribed tolerances; if not satisfied, repeat steps 2–5.
7. Output the pre-stressed structure displacement $\mathbf{u}_0$, with associated strain and Cauchy-stress fields in the solid and fluid.
8. Assemble the material stiffness matrix and the geometric stiffness matrix of the solid structure about $\mathbf{u}_0$.
9. Solve the geometrically nonlinear buckling eigenproblem.
10. Output positive buckling load factors λ_i and their mode shapes $\boldsymbol{\varphi}_i$.

The analysis in this work generates pre-stress from steady turbulent FSI and evaluates geometrically nonlinear buckling about pre-stress state. We do not model global wing-box bending or skin ovalization, and thereby Brazier-induced crushing loads are not included in the present case examples. To move forward to industrial applications, the workflow can be readily extended: a Brazier pre-stress field obtained from a separate thin shell or global bending analysis can be supplied as an additional load case in future work.

3. Optimization strategy

3.1. Optimization problem

We now formulate the design optimization for the aerodynamic structure. In a large-displacement FSI, the optimization problem belongs to the class of design dependent load problems. As the structure deforms, its surface geometry changes and therefore the pressure and shear distributions on that surface change.

To guarantee structural stability, we augment the conventional compliance minimization formulation with explicit buckling constraints. In stability oriented design we would ideally maximize the critical load multiplier λ, thereby improving resistance to buckling. Instead, in an optimization problem, it is convenient to work with its reciprocal. We define the reciprocal buckling load factor μ, as the inverse of the critical load multiplier λ_{crit} as follows.

$$\mu = \frac{1}{\lambda_{crit}} \tag{26}$$

A lower μ corresponds to a higher critical buckling load (i.e. better stability). Now Eq. (23) in Section 2.2 becomes:

$$[\mathbf{K}_\sigma(\boldsymbol{\alpha}, \mathbf{u}_0) + \mu \mathbf{K}_T(\boldsymbol{\alpha}, \mathbf{u}_0)]\boldsymbol{\phi} = \mathbf{0} \tag{27}$$

where the design variable $\boldsymbol{\alpha}$ defines the topology. $\alpha_j = 1$ indicates solid material and $\alpha_j = 0$ indicates void. The eigenvalue μ of Eq. (27) is solved as:

$$\mu = -\frac{\boldsymbol{\phi}^T \mathbf{K}_\sigma(\boldsymbol{\alpha}, \mathbf{u}_0)\boldsymbol{\phi}}{\boldsymbol{\phi}^T \mathbf{K}_T(\boldsymbol{\alpha}, \mathbf{u}_0)\boldsymbol{\phi}} \tag{28}$$

The corresponding eigenvectors $\boldsymbol{\phi}_i$ satisfy orthonormalization condition as follows.

$$\boldsymbol{\phi}_i^T \mathbf{K}_T(\mathbf{u}_0)\boldsymbol{\phi}_k = \delta_{ik} \tag{29}$$

where δ_{ik} is the Kronecker delta.

Mode switching phenomenon occurs in buckling based optimization when different buckling modes are associated with closely spaced or repeated buckling factors. This can lead to non-differentiable sensitivity expression and prevent optimization process from convergence. A common way to solve this issue is using aggregation functions. The maximum reciprocal buckling factor μ is obtained through a Kreisselmeier-Steinhauser (K-S) aggregation function [28], which uses an aggregating parameter ρ_{KS} to combine multiple individual buckling factors into a single differentiable expression (Eq. (30)). A standard buckling-constrained formulation simply requires that the aggregated μ_{KS} stays below a target value. However, mode switching is a common phenomenon where the critical buckling mode changes during the optimization process, resulting in unstable optimization [29–32]. This instability makes the optimization sensitive to the choice of ρ_{KS}. For instance, a large value of ρ_{KS} such as 300 can yield accurate approximation to the critical buckling factor but it results in mode switching and difficulty in convergence. A small value of ρ_{KS} such as 10 can stabilize the optimization process but may not incorporate the actual critical buckling mode effectively. To address these challenges and avoid extensive fine tuning of the aggregation parameter, an approach to decouple the critical buckling load factor from the aggregated function is adopted [32]. The buckling load constraints include two separate constraints: one directly on the first eigenvalue μ_1 and another on a KS-aggregated eigenvalues of the higher modes starting from the second load factor ($\mu_2, \mu_3, \ldots, \mu_q$). The aggregated buckling factor is expressed as:

$$\mu_{KS}^{2-q} = \mu_2 + \frac{1}{\rho_{KS}} \ln\left(\sum_{i=2}^{q} \exp(\rho_{KS}(\mu_i - \mu_2)) \right) \tag{30}$$

The overall topology optimization model minimizes the structural compliance subject to buckling and volume constraints.

$$\begin{aligned} &\text{Minimize}: C(\boldsymbol{\alpha}, \mathbf{u}) = \mathbf{u}^T \mathbf{K}_T(\boldsymbol{\alpha}, \mathbf{u}_0)\mathbf{u} \\ &\text{Subjectto}: \begin{cases} \mu_1 \lambda^* - 1 \le 0 \\ \mu_{KS}^{2-q} A\lambda^* - 1 \le 0 \\ V(\boldsymbol{\alpha}) = \dfrac{1}{|\Omega_s|}\displaystyle\int_{\Omega_s} \boldsymbol{\alpha} d\Omega \le V^* \\ \alpha_j \in \{0,1\}, \quad j \in [1, N_d], \quad \forall \alpha_j \in \Omega_s \end{cases} \end{aligned} \tag{31}$$

where the objective $C(\boldsymbol{\alpha},\mathbf{u})$ is the compliance, which is minimized to achieve a stiffer structure. The parameter λ^* specifies the allowable limit for the first buckling factor λ_1, and $A\lambda^*$ similarly set the bound for the aggregated higher modes. In other words, two buckling constraints are imposed by requiring that the first reciprocal buckling load factor μ_1 is below a prescribed threshold μ^* to ensure sufficient buckling strength, and the aggregated reciprocal buckling factor μ_{KS} is below a slightly higher threshold $A\mu^*$. After numerical tests, the parameter A=1.1 serves as a small safety gap between the first-mode constraint and the KS-aggregated constraint, preventing the optimization from potential switching between buckling modes during convergence. A volume constraint V^* restricts the total mass of material used or the actual volume fraction $V(\boldsymbol{\alpha})$. N_d denotes the number of elements in the design variable vector $\boldsymbol{\alpha}$, and design variables are binary in the solid domain (0 = void, 1 = solid). In this study, since the accuracy of the first buckling factor is not influenced by aggregation parameter ρ_{KS}, a small value of ρ_{KS}=10 is used in all numerical cases to improve optimization process.

3.2. Sensitivity analysis

The employed optimization method is a gradient-based method, so the derivatives of both the objective and constraint functions with respect to the design variables $\boldsymbol{\alpha}$ are required to be calculated at each design update. These are sensitivities and we compute them via the adjoint method [33], which avoids the prohibitively expensive direct evaluation of how the state variables U change with $\boldsymbol{\alpha}$. In this method, for a generic function $f(\boldsymbol{\alpha}, U)$ (whether it be the compliance or a buckling eigenvalue), we introduce the Lagrangian

$$\mathscr{L}(\boldsymbol{\alpha}, U, \nu) = f(\boldsymbol{\alpha}, U) + \nu^T \mathbf{R}(\boldsymbol{\alpha}, U) \tag{32}$$

where $\boldsymbol{R}(\boldsymbol{\alpha}, U) = 0$ represents the residual vector of the governing equations (structural equilibrium or eigenproblem), and ν is the adjoint variable vector. The sensitivity field of this function $\mathscr{L}$ is obtained by differentiating it with respect to $\boldsymbol{\alpha}$, which gives

$$\frac{d\mathscr{L}}{d\boldsymbol{\alpha}} = \frac{\partial f}{\partial \boldsymbol{\alpha}} + \frac{\partial f}{\partial U}\frac{dU}{d\boldsymbol{\alpha}} + \nu^T\left(\frac{\partial \mathbf{R}}{\partial \boldsymbol{\alpha}} + \frac{\partial \mathbf{R}}{\partial U}\frac{dU}{d\boldsymbol{\alpha}}\right) \tag{33}$$

$$\frac{d\mathscr{L}}{d\boldsymbol{\alpha}} = \frac{\partial f}{\partial \boldsymbol{\alpha}} + \nu^T\frac{\partial \mathbf{R}}{\partial \boldsymbol{\alpha}} + \left(\frac{\partial f}{\partial U} + \nu^T\frac{\partial \mathbf{R}}{\partial U}\right)\frac{dU}{d\boldsymbol{\alpha}} \tag{34}$$

Since evaluating $dU/d\boldsymbol{\alpha}$ is highly computationally expensive, it is common to set the bracketed term of Eq. (34) equal to zero,

resulting in the adjoint equation:

$$\frac{\partial f}{\partial U}+\nu^T\frac{\partial \mathbf{R}}{\partial U}=0 \tag{35}$$

Once ν is solved from Eq. (35), the final sensitivity formula is

$$f_\alpha=\frac{df}{d\boldsymbol{\alpha}}=\frac{\partial f}{\partial \boldsymbol{\alpha}}+\nu^T\frac{\partial R}{\partial \boldsymbol{\alpha}} \tag{36}$$

which is a general formulation to calculate the sensitivities of a generic function f.

For the specific cases of the compliance $C(\boldsymbol{\alpha})$ and the ith buckling reciprocal $\mu_i(\boldsymbol{\alpha})$, their sensitivities are calculated in Eq. (37) and Eq. (38), respectively.

$$\frac{dC(\boldsymbol{\alpha})}{d\boldsymbol{\alpha}}=\frac{\partial C(\boldsymbol{\alpha})}{\partial \boldsymbol{\alpha}}+\nu^T\frac{\partial R}{\partial \boldsymbol{\alpha}} \tag{37}$$

$$\frac{d\mu_i(\boldsymbol{\alpha})}{d\boldsymbol{\alpha}}=\frac{\partial \mu_i(\boldsymbol{\alpha})}{\partial \boldsymbol{\alpha}}+\nu^T\frac{\partial R}{\partial \boldsymbol{\alpha}} \tag{38}$$

The used semi-automatic differentiated sensitivities calculation for FSI with geometric non-linearity and turbulent flow has been validated through finite difference method [34,35]. It is noted that design sensitivities are computed via a discrete adjoint of the coupled analysis that differentiates the RANS momentum, continuity and the k-ε transport equations. For the accuracy of the computed gradients, frozen turbulence assumption is not used in this case.

Then the KS-aggregation eigenvalue sensitivities, as shown in Eq. (39), are computed as [36,37]

$$\frac{\partial \mu_{2-q}^{KS}}{\partial \boldsymbol{\alpha}}=\frac{\sum_{i=2}^{q}\left(\exp(\rho(\mu_i-\mu_2))\frac{\partial \mu_i}{\partial \boldsymbol{\alpha}}\right)}{\sum_{i=2}^{q}\exp(\rho(\mu_i-\mu_2))} \tag{39}$$

After obtaining all required gradients of compliance at iteration k, individual buckling factors and KS aggregate, the total sensitivity is calculated by combining them using two augmented Lagrangian multipliers Λ_1 and Λ_2, as given by Eq. (40)

$$\frac{\partial f(\boldsymbol{\alpha})}{\partial \boldsymbol{\alpha}}=\frac{\partial C(\boldsymbol{\alpha})}{\partial \boldsymbol{\alpha}}+\Lambda_1\frac{\partial \mu_1(\boldsymbol{\alpha})}{\partial \boldsymbol{\alpha}}+\Lambda_2\frac{\partial \mu^{KS}(\boldsymbol{\alpha})}{\partial \boldsymbol{\alpha}} \tag{40}$$

where Λ_1 and Λ_2 themselves update according to:

$$\Lambda_1=\begin{cases}0 & \text{if}\lambda_1>\lambda^*\text{and}\omega=0\\ \dfrac{0.05\gamma^k\times\left(\lambda^*-\lambda_1^k\right)+0.95\gamma^{k-1}\left(\lambda^*-\lambda_1^{k-1}\right)}{\lambda^*} & \text{if}\lambda_1\le\lambda^*\text{or}\omega=1\end{cases} \tag{41}$$

$$\Lambda_2=\begin{cases}0 & \text{if}\lambda_2>A\lambda^*\text{and}\omega=0\\ \dfrac{0.05\gamma^k\times\left(A\lambda^*-\lambda_2^k\right)+0.95\gamma^{k-1}\left(A\lambda^*-\lambda_2^{k-1}\right)}{A\lambda^*} & \text{if}\lambda_2\le A\lambda^*\text{or}\omega=1\end{cases} \tag{42}$$

in which γ^k is the current kth iteration Lagrangian multiplier. A Boolean flag ω tracks whether buckling constraints have been activated ($\omega=1$) or not ($\omega=0$). Buckling constraint is triggered as soon as the computed buckling factor first falls below its prescribed limit; thereafter it remains active for the rest of the optimization, ensuring that Λ remains continuous. After each step, γ is adjusted by the following formula:

$$\gamma^{k+1}=\begin{cases}\gamma^k\times\eta & \text{when}\Delta\lambda>0.1\%\\ \gamma^k/\eta & \text{when}\Delta\lambda<-0.1\%\\ \gamma^k & \text{otherwise}\end{cases} \tag{43}$$

where η is an update coefficient. η is predefined as 1.01 and γ^0 is set to 1 based on numerical experiments. The difference between computed and constrained buckling factor values is calculated as $\Delta\lambda$, with $\Delta\lambda=(\lambda^*\text{-}\lambda_1)/\lambda^*$ and $\Delta\lambda=(A\lambda^*\text{-}\lambda_2)/A\lambda^*$ for use in Λ_1 and Λ_2, respectively. Whenever the computed buckling factor undershoots the prescribed buckling constraint by a small percentage, we increase γ by multiplying it by η. Conversely, if the computed factor greatly exceeds the defined constraint, γ is down-scaled by the same update coefficient. If neither condition holds, γ remains unchanged. Finally, to improve the optimization stability and convergence, the sensitivity field is smoothed by taking a moving average over the current and last three iterations, as follows:

$$f_\alpha=\frac{f_\alpha^k+f_\alpha^{k-1}+f_\alpha^{k-2}+f_\alpha^{k-3}}{4} \tag{44}$$

In order to compute the derivatives of the structural compliance and buckling factors, we need to interpolate the physical model in

terms of the topology design variables. For the solid domain, we adopt the SIMP material model which is expressed as

$$E(\alpha_j) = \alpha_j^p E_0 \quad \text{on} \quad \Omega_s, \tag{45}$$

where E_0 is the Young's modulus of the bulk material and E represents the interpolated property with respect to design variable α_j. We choose the penalization exponent p=3 to be sufficient to drive α toward true 0–1 designs.

3.3. Discrete topology optimization method

To take advantage of naturally eliminating the pseudo buckling mode issues from the optimized design, a discrete topology optimization method is used. Specifically, we employ the Topology Optimization of Binary Structures with Geometry Trimming (TOBS-GT) method [38] to solve the {0, 1} design problem. With a clear solid/void material distinction, it also aligns directly with manufacturing realities.

To solve the optimization problem in Eq. (31), we use the TOBS algorithm [39], which generates a sequence of integer linear subproblems via linear approximations. At each iteration k, generic objective $f(\boldsymbol{\alpha})$ and constraint $g(\boldsymbol{\alpha})$ functions are linearized by a first-order Taylor series expansion about the design variable $\boldsymbol{\alpha}^k$:

$$\begin{aligned} f(\boldsymbol{\alpha}) &\approx f(\boldsymbol{\alpha}^k) + \frac{\partial f(\boldsymbol{\alpha}^k)}{\partial \boldsymbol{\alpha}} \cdot \Delta\boldsymbol{\alpha}^k + O(\parallel \Delta\boldsymbol{\alpha}^k \parallel_2^2) \\ g(\boldsymbol{\alpha}) &= g(\boldsymbol{\alpha}^k) + \frac{\partial g(\boldsymbol{\alpha}^k)}{\partial \boldsymbol{\alpha}} \cdot \Delta\boldsymbol{\alpha}^k \end{aligned} \tag{46}$$

where $\Delta\boldsymbol{\alpha}^k$ is the vector of design variable updates and $\parallel \Delta\boldsymbol{\alpha}^k \parallel_2^2$ denotes the higher-order terms or truncation error. There is no error associated with the constraint function because its variation is linear.

As the densities of design variable $\boldsymbol{\alpha}^k$ is maintained binary, each update $\Delta\boldsymbol{\alpha}^k$ is constrained to {-1, 0} if the element is currently solid ($\boldsymbol{\alpha}_j$ =1) or to {0, 1} if it is void ($\boldsymbol{\alpha}_j$ =0). This is defined via bound constraints in the subproblem:

$$\Delta\boldsymbol{\alpha}^k = \begin{cases} 0 \le \Delta\boldsymbol{\alpha}^k \le 1, & \text{if} \boldsymbol{\alpha}_j^k = 0 \\ -1 \le \Delta\boldsymbol{\alpha}^k \le 0, & \text{if} \boldsymbol{\alpha}_j^k = 1 \end{cases} \tag{47}$$

In Eq. (46), the higher order terms $\parallel \Delta\boldsymbol{\alpha}^k \parallel_2^2$ for the objective function are neglected because the integer linear programming problems are created using linear approximation in the TOBS method. To ensure that the linearization remains valid, a parameter β is introduced to control only the number of elements βN_d changing between solid and void in each iteration. This constraint is written as:

$$\parallel \Delta\boldsymbol{\alpha}^k \parallel_1 \le \beta N_d \tag{48}$$

Based on the linearized functions (Eq. (46)), the kth integer linear subproblem becomes

$$\begin{aligned} &\text{Minimize} \quad \frac{\partial C(\boldsymbol{\alpha}^k)}{\partial \boldsymbol{\alpha}} \cdot \Delta\boldsymbol{\alpha}^k \\ &\text{Subjectto} \quad \frac{\partial V(\boldsymbol{\alpha}^k)}{\partial \boldsymbol{\alpha}} \cdot \Delta\boldsymbol{\alpha}^k \le \overline{V} - V(\boldsymbol{\alpha}^k) = \Delta V^k, i \in [1, N_g] \\ &\parallel \Delta\boldsymbol{\alpha}^k \parallel_1 \le \beta N_d \\ &\Delta\boldsymbol{\alpha}_j^k \in \left\{ -\boldsymbol{\alpha}_j^k, 1 - \boldsymbol{\alpha}_j^k \right\}, \quad j \in [1, N_d] \end{aligned} \tag{49}$$

where ΔV^k is the allowed volume change at iteration k. $\boldsymbol{\alpha}_j^k$ is the design variable of the jth element at iteration k. Once the optimum change $\Delta\boldsymbol{\alpha}^k$ is found, we update design variables as

$$\boldsymbol{\alpha}^{k+1} = \boldsymbol{\alpha}^k + \Delta\boldsymbol{\alpha}^k \tag{50}$$

The added constraint in Eq. (48), only allows small volume change in the design variables at iteration k [40]. Therefore there can be situations when some of the subproblem's volume constraints become infeasible because the bound $\Delta V_i^k = \overline{V} - V(\boldsymbol{\alpha}^k)$ needs a large step to find a feasible solution. To ensure a viable solution at each iteration, the upper bounds of the constraints ΔV^k is relaxed using a relaxation parameter ε corresponding to the volume constraint, following the rules:

$$\Delta V^k = \begin{cases} -\varepsilon_i V(\boldsymbol{\alpha}^k) & \text{if} \overline{V} < (1 - \varepsilon_i) V(\boldsymbol{\alpha}^k), \\ \overline{V} - V(\boldsymbol{\alpha}^k) & \text{if} \overline{V} \in \left[(1 - \varepsilon_i) V(\boldsymbol{\alpha}^k), (1 + \varepsilon_i) V(\boldsymbol{\alpha}^k) \right], \\ \varepsilon_i V(\boldsymbol{\alpha}^k) & \text{if} \overline{V} > (1 + \varepsilon_i) V(\boldsymbol{\alpha}^k). \end{cases} \tag{51}$$

where the relaxation parameter ε gradually modifies the bound values based on neighboring values of the current volume constraint. These values ε and β are from the TOBS method are selected based on numerical experience. Typical values from the literature for ε are from 0.005 to 0.02 and for β are 0.01 to 0.05 [35]. In this work, small values $\varepsilon = 0.005$ and $\beta = 0.01$ are chosen in all cases, which are

numerically tested to be effective for this buckling-constrained optimization.

Beyond standard formulations, we build a discrete topology optimization scheme where at each design iterate a RANS based turbulent FSI analysis with ALE mesh motion and a total Lagrangian large deformation solid model deliver the pre-stressed state. From this state we assemble the tangent and geometric stiffness and solve a geometrically nonlinear buckling eigenproblem. The resulting critical buckling load factor is enforced as an active constraint by the optimizer. This tight coupling addresses stability under realistic aerodynamics without grey element artifacts. To the best of our knowledge, no prior discrete topology study has coupled a RANS turbulent solver and a large-deformation solid within an optimization framework.

4. Numerical implementation

The developed algorithm extended a material distribution method with stability parameter to optimize stable aerodynamic structures. Compared to the conventional study in minimizing compliance or mass, the buckling mechanism has been added to the design problem. All codes for this study are developed using MATLAB. COMSOL Multiphysics is integrated with MATLAB via the LiveLink for MATLAB.

The optimization framework consists of the optimizer and physics solver, which are decoupled and considered as individual modules. In each iteration, the fully coupled fluid–structure equilibrium equations are solved with a segregated finite element solver in COMSOL Multiphysics, treating the fluid and solid subdomains independently and iterating until convergence. In the software, the RANS equations containing the standard k-ε turbulence model are computed with the standard wall functions. The software also returns the necessary compliance and buckling sensitivities via its semi-automatic symbolic differentiation tools. The material models are implemented by editing the material properties and stress coupling condition.

The TOBS-GT method encodes the design on a grid of binary variables (1=material, 0=void) to communicate with the FEA modules. A geometry trimming (GT) procedure is a process of creating a CAD geometry by firstly reading the binary design variables and then trimming out the original CAD domain accordingly. The binary design variables 1 and 0 prescribes the presence and absence of material respectively. The GT procedure creates an updated model that exactly captures the new topology contours, and this procedure is illustrated in Fig. 2. The smoothing contour procedure is to apply a nodal filter to the distribution of design variables [35].

Same physics-controlled FEA meshes are used for FSI and buckling analysis. The computational meshes employ triangular elements in the solid domain and most of the fluid domain and use quadrilateral elements to resolve boundary layers for turbulent flow. The shape functions used include quadratic Lagrange interpolation for the structural displacements, quadratic velocity and linear pressure discretization for the fluid. Fluid boundary layer grids is employed. The maximum element size in the FEA mesh is limited to four times the optimization grid spacing. Adaptive mesh refinement is used to improve local solutions. Specifically, the built-in parameter in the software used to control element sizes is set to 3000 so that small structural members are computed accurately. Additional information of the optimization and FEA mesh is given in Section 5.

The analyses are performed assuming plane stress. COMSOL's FSI module uses an ALE scheme to handle the moving fluid–solid interface. In ALE, the fluid equations are solved on a fixed spatial grid (Eulerian frame), while the solid mechanics are based on a material grid that deforms with the structure (Lagrangian frame). Our optimization grid is attached to the material frame, so we extract sensitivity information from the structure's deformed configuration, as shown in Fig. 3.

To use the semi-automatic differentiation in COMSOL, the structural mean compliance objective is defined as Global Objective 1 with the expression solid.Ws_tot. The reciprocal buckling load factor used in the optimization is defined as Global Objective 2 with the expression 1/solid.LFcrit. Elementwise sensitivities are returned by the discrete-adjoint module as the pointwise field fsens(p1)/dvol, where p1 is the control variable defined in the Control Variable Field and dvol normalizes by the local element volume. For buckling, the eigenproblem is assembled about the converged FSI pre-stress state, and the sensitivity engine differentiates the material and geometric stiffness operators. The pointwise sensitivities are extracted on a rectangular grid coincident with the optimization grid. The higher mode buckling load factor sensitivities are aggregated in MATLAB through KS aggregate function. Using the respective sensitivities, the optimizer finally updates binary design variables {0,1}.

To deal with potential simulation divergence when the breakage of thin structural members leads to very large local deformation during optimization process, we include an optional linear structural analysis to supplement the nonlinear FSI solver. Specifically, each iteration starts with the nonlinear FSI analysis. Only if that fails do we switch to a linearized solver for that step and then continue the following buckling analysis and the optimization loop. In practice, linear analysis was activated only a few times in the FSI analysis of very limited examples and not needed at all in buckling analysis. In addition, all problems converged in the nonlinear regime. In all cases, convergence is achieved when the average change of the objective over 10 consecutive iterations falls below the tolerance τ=0.001 [40,41]. A summary of our overall algorithm is presented below.

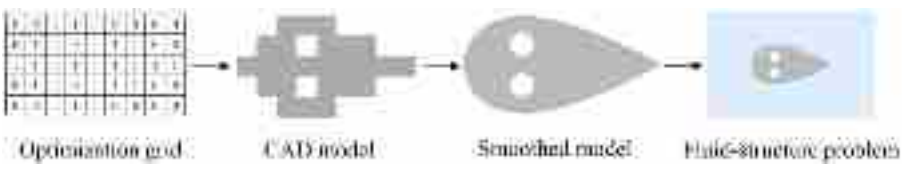

Fig. 2. Representation of the geometry trimming (GT) procedure and smoothing. A highly coarse grid is purely for conceptual clarity and the actual optimization and trimming steps operate on a much finer mesh.

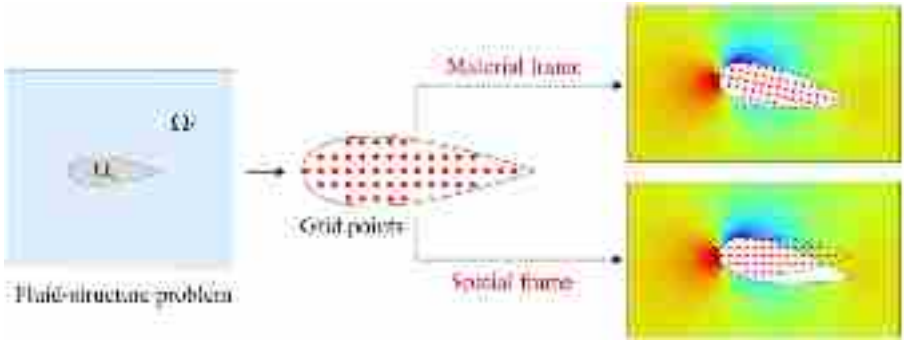

Fig. 3. Binary topology optimization grid computed in the material frame with mapping to the spatial frame.

1. Initialize parameters for finite element models and optimization inputs;
2. Generate optimization mesh and assign {0,1} design variables;
3. Create CAD files of holes by reading the topology information and trimming out the void regions;
4. Meshing the geometry from the CAD model;
5. Solve FSI analysis equations;
6. Solve buckling analysis equations based upon displacement and stress fields from the FSI analysis;
7. Extract sensitivities at design grid point, mapping between the spatial and material frames;
8. Calculate the augmented Lagrangian multipliers;
9. Filter and average the sensitivity values;
10. Solve the integer linear programming problem;
11. Update design variables to generate new binary topology;
12. Stop the optimization if converged. If not converged, return to step 3 and iterate.

5. Numerical examples

The effectiveness of the proposed framework is demonstrated through a NACA 0030 airfoil. This publicly parameterized NACA 0030 section is used to provide adequate interior thickness for meaningful rib topology and different topologies can be clearly visualized under varying levels of buckling constraint. We present three test cases with different flow velocities, FSI boundary conditions and angles of attack (AoA). Various levels of buckling constraint are evaluated in all the cases to validate our approach and evaluate their influence on the resulting topology.

In all optimizations, the developed method successfully achieved buckling-constraint designs beginning from a fully solid domain instead of evolving based on compliance minimization design to avoid biasing in exploring all possible design configurations. Simulations were carried out on a workstation equipped with an Intel Core i9–14900K CPU @ 3.2 GHz, having 24 cores and 128 GB memory. A total of 32 threads are used in parallel computation for the finite-element analyses.

5.1. Case I: zero AoA with sides fixed

As shown in Fig. 4, we test our approach on the solid airfoil embedded within a fluid domain, which consists of a semicircle with radius of 10 m and a rectangle with width of 10 m and height of 20 m. The top, left and bottom walls are set as inlet Γ_{in}, imposing a

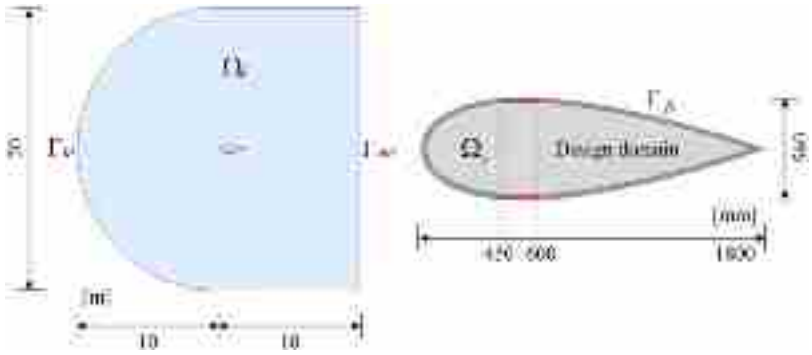

Fig. 4. Schematic of design domain and boundary conditions for the airfoil optimization. Dimensions of the fluid (left) and solid (right) domain are given in meter and millimeters, respectively.

uniform velocity entering from the left, with a default turbulent intensity of 0.05 and a turbulence length scale of 0.01 m. The flow velocity is determined by Reynolds number *Re*, which is set to 1×10^4 and 2×10^4 based on the chord length as its characteristic length. The right boundary of the fluid domain is an outlet Γout, imposed with a zero normal stress boundary condition. The side of the wing skin, 450 to 600 mm from the leading edge, is structurally fixed with zero displacement as shown in red color in Fig. 4. The airfoil has a chord length of 1.8 m and a width equal to one third of its length. The airfoil operates at its minimum drag with zero angle of attack when it travels at high speed. The fluid density is set as $1.225 kg/m^3$. The compliant airfoil is assigned by solid material with properties of Young's modulus of $E = 10$ MPa and a Poisson's ratio of $\nu = 0.37$ in this case. A filter radius equal to ten grid spacings is used as the optimization parameter.

The structural component is discretized into 600×180 optimization elements with the material outside the airfoil boundary removed. The goal is to optimize the internal geometry of the structure. A non-design layer is set on the inner surface of the airfoil with a small thickness of five elements.

For the purpose of comparing compliance-only design and buckling-constraint formulation, the identical setup and same optimization parameters are used for analysis. In addition, to compare the numerical buckling constrained results and the results without buckling constraints, we normalize every buckling eigenvalue λ by the first mode value λ_1 from the pure compliance design. Hence $\lambda^* = \lambda/\lambda_o$ is presented as a nondimensional ratio instead of an absolute eigenvalue.

The proposed method can deal with different turbulent flow velocities without the need of changing its algorithm. Fig. 5 presents the flow fields around the compliant airfoil whose internal topology has been optimized with a buckling constraint $\lambda^* = 2$, at two Reynolds numbers. Comparing the optimized designs between the left and right figures, almost same internal topologies are produced with different aerodynamic velocities, except for minor differences on size of holes. In both velocity cases, the compliant leading edge is pushed downstream by the aerodynamic loads, whereas the trailing edge is stretched longer. When the Reynolds number doubles (Fig. 5 (b) and (d)), higher flow speeds contribute to pressure asymmetry and bending occurs on compliant members close to the trailing edge.

The highest buckling constraint lower bound applied with convergence is $\lambda^* = 3.5$ on the lower Reynolds number case. Its intermediate solid structure contours during optimization are shown in Fig. 6. The structure in Fig. 6 (a) is the first optimization step start with a full design domain. From the intermediate solid structure contours, it can be seen that the method is able to self-nucleate holes. The holes are firstly created in the middle section and trailing edge of the airfoil and then propagate to the leading edge. In the final optimal result, a O-shaped bracket is developed at the trailing edge.

The convergence curves of the numerical example with highest buckling constraint $\lambda^* = 3.5$ is plotted in Fig. 7, including the value of compliance *C*, the first four orders of buckling factors λ_1 to λ_4 and volume fraction *V*. It can be found that the convergence process during optimization process is steady. Peaks occur occasionally when internal members break up during topology evolution process. When the internal material of the airfoil is gradually removed in the first 100 iterations, thin members are generated, resulting in a decrease of both structural stiffness and buckling factors. After that when the target mass reduction is met, the algorithm gradually distribute material from the airfoil leading edge to the trailing edge and evolve more stable members, shown from Fig. 6 (f-h). This results in the effective increase of the first buckling factor to meet the prescribed buckling lower bound.

Fig. 8 compares the first buckling mode shapes of the pure compliance design (left) and the $\lambda^* = 3.5$ buckling constrained design

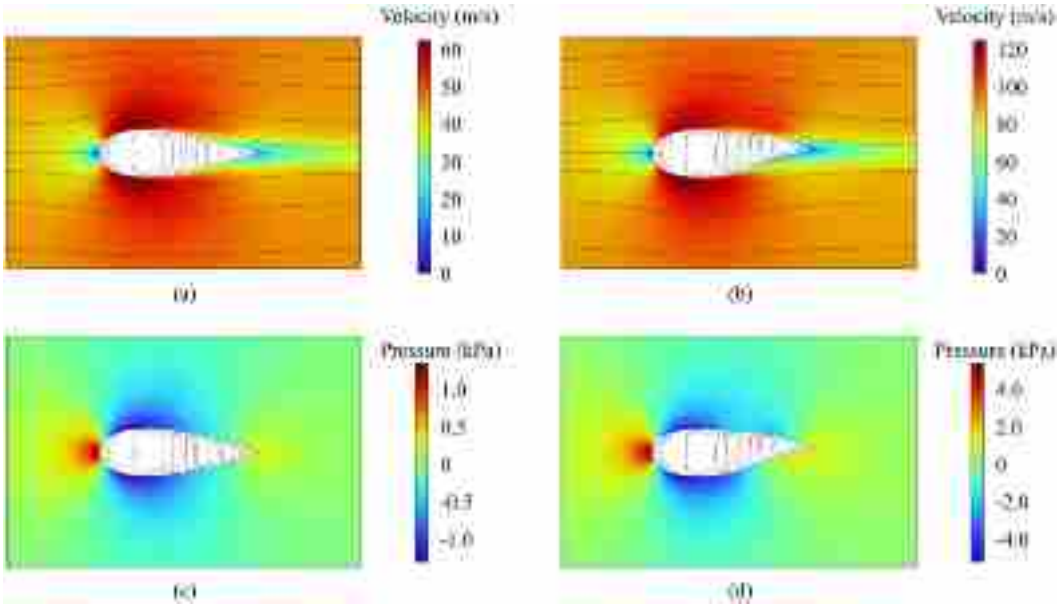

Fig. 5. Velocity magnitude and pressure field for the optimized design with the normalized buckling constraint λ^*=2 under $Re = 1 \times 10^4$ in (a) and (c), and $Re = 2 \times 10^4$ in (b) and (d).

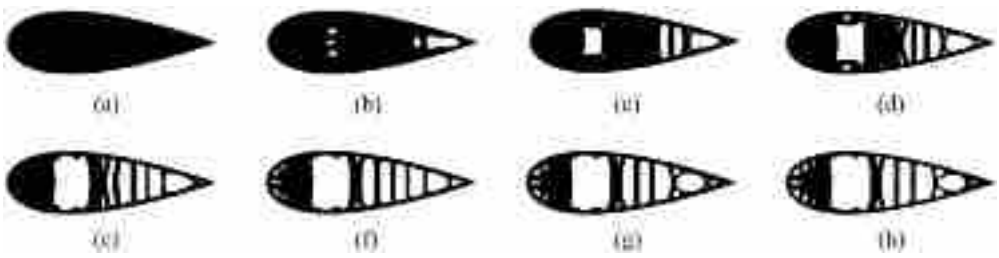

Fig. 6. Topology evolution during the iterative buckling constraint optimization for $Re = 1 \times 10^4$ with normalized buckling constraint $\lambda^* = 3.5$ at (a) iteration 1, (b) iteration 8, (c) iteration 20, (d) iteration 40, (e) iteration 75, (f) iteration 150, (g) iteration 660, (h) iteration 943.

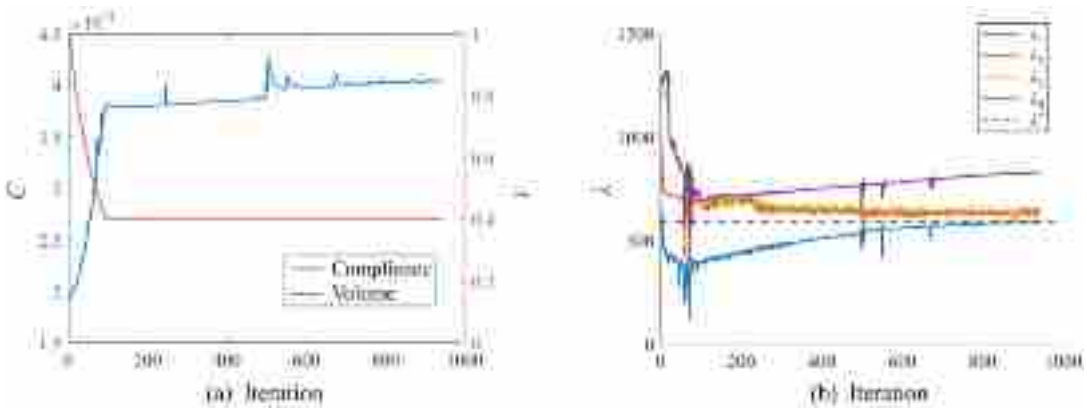

Fig. 7. Convergence history curves for the objective and constraint functions (a) compliance and volume fraction (b) absolute buckling load factors λ_1–λ_4 for the optimized designs, with the dashed line marking the normalized constraint $\lambda^* = 3.5$ (i.e. 3.5 × the first-mode eigenvalue of the pure-compliance design).

(right). In the compliance only design, the dominant instability exhibits at the entire thin trailing edge. However, in the high buckling constraint enforced design, the critical buckling mode changes and it is highly localized, occurring only at the trailing tip. The first buckling factor from this buckling constrained design is 646.0, which is close to the 591.2 value of the original full solid domain before optimization. This demonstrates the effectiveness of the optimization method in maintaining the structural stability while reducing the airfoil's mass.

The optimization designs and corresponding numerical results for various buckling constraints are shown in Fig. 9, including the compliance minimization design for comparison purposes. Overall, at the front of the airfoil internal structures are oriented perpendicular to the surface tangent to resist upstream flow impact. In the rear part of the airfoil, several vertical members and X-shaped braces are generated to resist compressive fluid load. As the buckling constraint λ^* increases from 1.5 to 3.5, web-shaped components are strategically formed at the trailing edge to enhance structural stability. It is found that introducing relatively lower buckling constraints can slightly increase the stiffness. This could be explained by the change in tangent stiffness matrix from the geometric nonlinearity in Eq. (27). When material is added in the compressed region to satisfy the buckling limit, not only the material stiffness $\mathbf{K}_{\text{mat}}$ but also the geometric stress stiffening term $\mathbf{K}_{\text{geom}}$ is amplified. Together they make the entire structure much stiffer, lowering displacements and compliance. Fig. 10 compares the percentage changes in the first buckling factor λ_1 and the compliance C for different levels of buckling constraints, each referenced to the compliance design baseline. It demonstrates that imposing a buckling constraint can substantially improve its structural stability (up to 250 %) while incurring only a minor compliance increase. For higher buckling constraints, compliance is slightly increased with reference to the compliance minimization design. While the relationship

Fig. 8. The first order buckling mode of the designs via compliance minimization and with normalized buckling constraint $\lambda^* = 3.5$. The coloring scheme indicates buckling mode displacement: dark purple color denotes large displacement and the light green color represents small displacement.

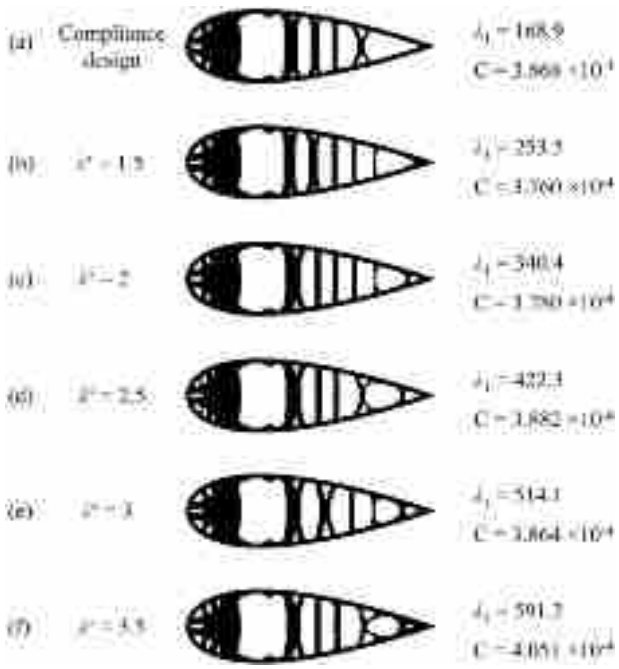

Fig. 9. Final optimized designs under various buckling constraints: (a) compliance minimization design; (b) $\lambda^* = 1.5$; (c) $\lambda^* = 2.0$; (d) $\lambda^* = 2.5$; (e) $\lambda^* = 3.0$; (f) $\lambda^* = 3.5$.

between compliance and buckling factor is non-monotonous in this case, overall increasing the buckling factor compromises the stiffness in the design.

5.2. Case II: zero AoA with middle fixed

In practical wing construction, airfoil skins and internal structures can be often bolted to the main spar in different locations. Such local attachments produce different structural boundary conditions. To demonstrate its feasibility in our topology optimization, an alternative FSI boundary condition is now considered, in which the airfoil skin is clamped only at a single mid-chord section rather than along both sides. As illustrated in Fig. 11, the design domain almost includes the entire interior of the NACA 0030 profile, except for a thin non-design layer. The fixed FSI interface is located 235 mm away from the leading edge. A volume bound of 50 % is imposed

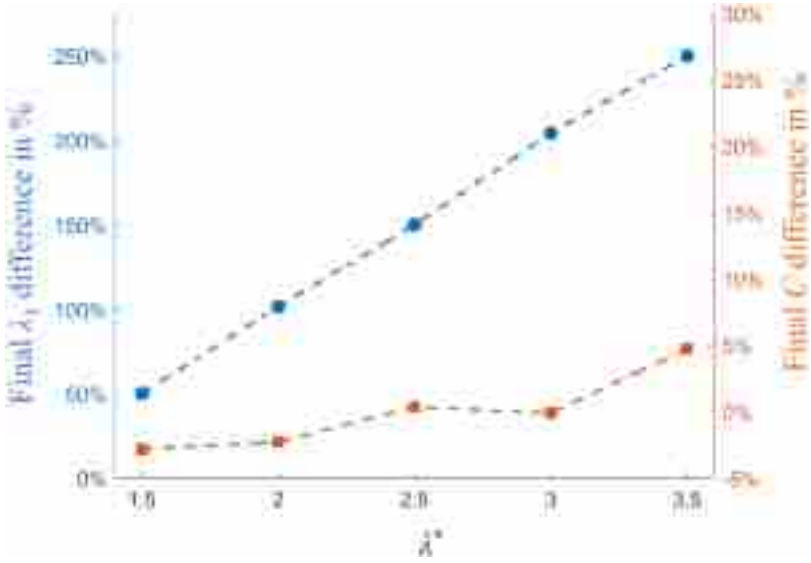

Fig. 10. Percentage of increase in critical buckling load factor and compliance, with references to the values from the compliance design.

in optimization. Reynolds number is set as $Re = 1 \times 10^4$. Fluid domain set up and optimization parameters are kept the same as in Case I. Starting from a fully solid domain, the optimization process converged in 203 and 224 iterations for $\lambda^* = 1.5$ and $\lambda^* = 2.0$. As it can be seen from Fig. 12, in contrast to Case I, significantly more materials are allocated to the mid chord region of the airfoil to resist compressive fluid loads and reinforce the fixed FSI point. Comparing to the compliance only layout in (a), the added buckling constraints (b) and (c) drive the algorithm to alter the X-shaped web close to the trailing edge into multiple slender vertical members. The reconfigurations in $\lambda^* = 1.5$ and $\lambda^* = 2.0$ increase the first buckling factor by about 50 % and 100 % while having only a minor impact on compliance (9 % and 7 %).

5.3. Case III: 30° AoA with sides fixed

We further assess robustness of our buckling constrained formulation by subjecting the NACA 0030 airfoil to a 30° angle of attack. By optimizing the design to exceed its stall angle, we ensure our method remains effective when the design is aimed at satisfying severe aerodynamic loading. A volume bound of 40 % is used in this case. Fluid boundary conditions, solid domain set up and optimization parameters are the same as in Case I. Starting from a fully solid domain, the optimization process converged in 239 and 682 iterations for $\lambda^* = 1.2$ and $\lambda^* = 1.4$. In this case, any buckling constraint above $\lambda^* = 1.4$ becomes infeasible due to the fact that once all available material has been optimally redistributed under the fixed volume limit, no further increases in stability are possible. Fig. 13 shows the velocity and pressure distributions respectively. It can be seen that both flow streamlines and pressure on the upper and lower surfaces are asymmetric. A large wake region occurs in the downstream region starting right behind the airfoil. The pressure at the lower surface is greater than that on the upper side. As a result, this pressure imbalance generates a net bending moment that yields the large downward displacement on lower trailing-edge skins, as can be seen from the optimized design. The observed deformation mode aligns well with published findings [42].

In the present steady external flow cases we employ the RANS k-ε model for multiple purposes including its robustness, lower computational cost and to enable a direct comparison between low and high angle-of-attack cases. The standard k-ε model has limitations and the size and reattachment of the separated region should be viewed qualitatively. Our focus here is the optimization framework, which does not depend on a particular turbulence model. When quantitative accuracy of the separated loads is required, other turbulence models can be used within the same workflow and with the same sensitivity computations.

Fig. 14 shows the final topologies for Case III (30° AoA, both sides fixed), along with their first buckling factor and compliance values. In the compliance design, slender and asymmetric members concentrate on the high pressure lower surface. However, the large upward bending moment on the right side induces compressive stress along the upper skin, resulting in a global buckling mode on the right section (Fig. 15). After applying the buckling constraint $\lambda^* = 1.2$, an additional small, inclined member is generated connecting the upper surface and the central slender bar, directly counteracting that bending moment and elevating λ_1. In the buckling constraint design $\lambda^* = 1.4$, the inclined connecting member extends to the next slender rib and also thickens, forming a more stable load path network. This more stable framework not only increases the original mode's critical load but also pushes that buckling shape above a new front-located mode, which now becomes the first eigenmode. In comparison to the compliance design, the first buckling load factors for the two buckling constraint designs have greatly increased by 20 % and 40 %, correlating to minor compliance variations of 5.6 %, 2.5 %, respectively.

The mesh created by COMSOL Multiphysics for the optimized design of the $\lambda^* = 1.4$ including fluid and solid domain is shown in Fig. 16. The CAD geometry trimming method enables the meshes to be freely created and meet the physical requirements. Most of the computational domain consists of triangular elements. The fluid domain at the fluid–structure interface is resolved using quadrilateral elements with $y+ \approx 1$. High element density concentrates around thin solid elements and high-stress regions, while coarser meshes are located in lightly loaded areas, minimizing total degrees of freedom without sacrificing local resolution during FEA solving process. Because the topology changes at every optimization step, a new mesh is generated for each design iteration.

As can be noticed in Fig. 17, mesh generation time increases during the first approximate 100 iterations, as the optimizer resolves the many small holes that emerge early in the topology evolving process. In our proposed topology optimization framework, the topology optimization process costs less than three percent of total computational calculation time. The computational bottleneck of the present algorithm is still the finite element analyses, which is expected in topology optimization methods when solving high fidelity physics [35]. The FSI solver requires more time than the eigenvalue problem solver mainly because it fully couples the solid and fluid domains and handles the moving mesh via the ALE method. The geometrically nonlinear buckling step, assembled from the FSI

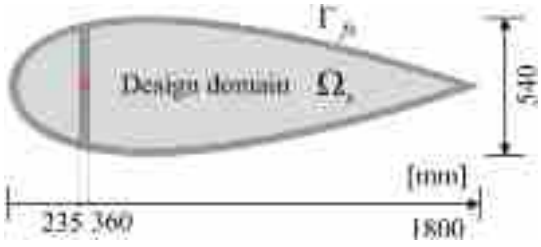

Fig. 11. Schematic of Case II showing the design domain (light gray), the non-design region (dark gray), and the fixed FSI boundary (red). Dimensions are given in millimeters.

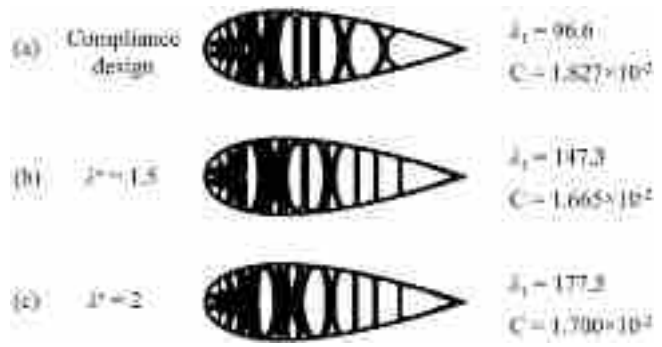

Fig. 12. Final optimized internal topologies for Case II (fixed mid-chord support) under different buckling constraints.

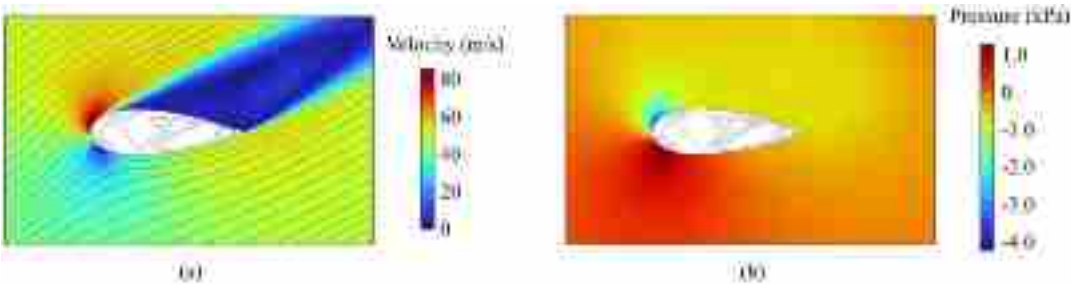

Fig. 13. Flow-field around the buckling-constrained optimized airfoil $\lambda^* = 1.2$ of Case III: at 30° AoA with both-sides fixed FSI support under $Re = 1 \times 10^4$ (a) Velocity magnitude (m/s) with streamlines; (b) Pressure field (kPa).

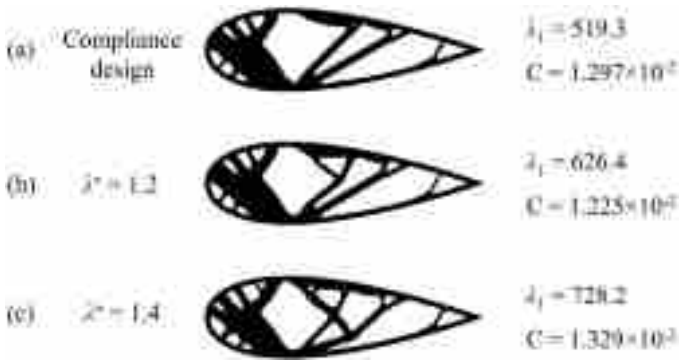

Fig. 14. Final optimized internal topologies for Case III (at 30° AoA) under different buckling constraints.

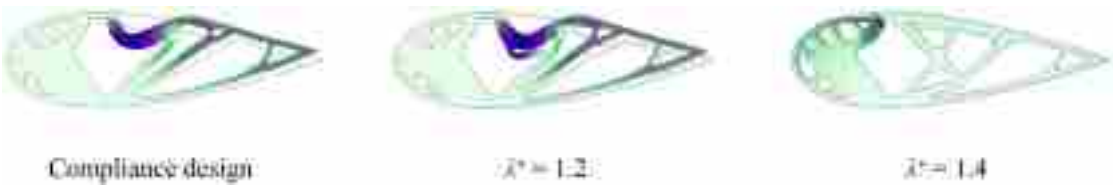

Fig. 15. The first order buckling mode of the designs via compliance minimization and with normalized buckling constraints $\lambda^* = 1.2$ and $\lambda^* = 1.4$. The coloring scheme indicates buckling mode displacement: dark purple color denotes large displacement and the light green color represents small displacement.

pre-stress state, adds a modest and relatively steady computational cost per iterate. The binary update, CAD geometry trimming, and remeshing procedures contribute minor and almost constant costs compared with the FEA solvers. An important efficiency feature is the separation of the optimization grid from the finite element analysis mesh: the optimization grid can be refined to capture fine

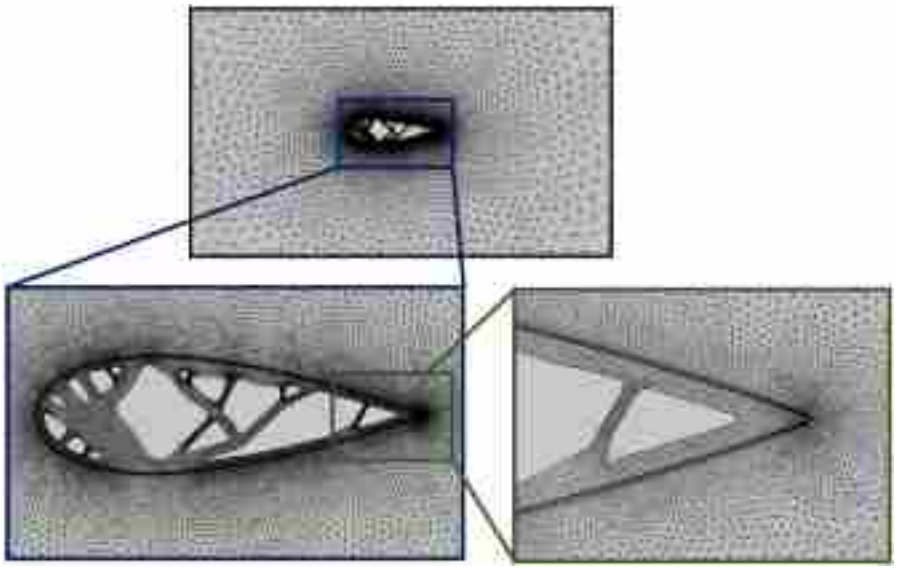

Fig. 16. Zoomed details of finite element mesh adaptive to the physics with body-fitted feature, containing 43,375 triangular and 1667 quadrilateral FSI boundary elements in the last optimization iteration with normalized buckling constraint λ^*=1.4.

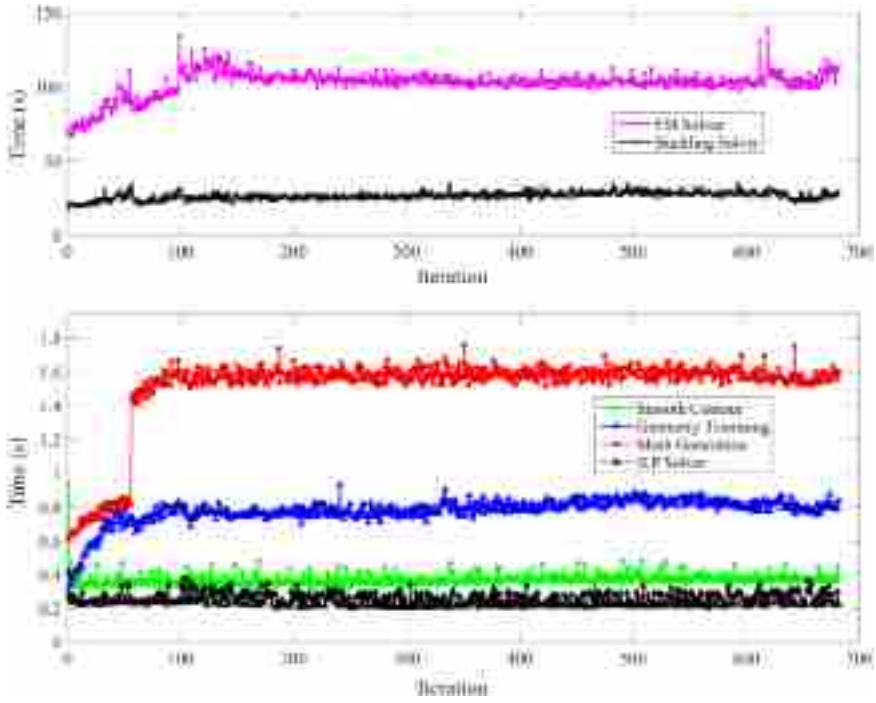

Fig. 17. Computation time cost breakdown per iteration over the $\lambda^* = 1.4$ optimization using TOBS-GT method.

topological changes, while the body fitted solid mesh and near wall fluid mesh refinement can be kept at a size that is computationally convenient for the coupled FSI and buckling analyses. In practice, coarser global meshes with appropriate boundary layer refinement reduce total runtime without degrading topological resolution, whereas large global refinement amplifies the FEA bottleneck. The representative case III was run on Intel Core i9–14900K CPU @ 3.2 GHz, 24 core, 128 RAM, with a total runtime of about 24 hours. The updates of the developed augmented Lagrange multipliers and augmentation penalty terms for buckling constraints update almost instantaneously, and the integer linear programming solver takes less than one second, demonstrating that the extended TOBS-GT method remains computationally efficient despite the inclusion of turbulent FSI and geometrically nonlinear buckling analyses.

In summary, the proposed buckling constraint TOBS-GT framework consistently enforces aerodynamic buckling constraints across

all test cases while generating lightweight, manufacturable topologies. The internal structures self-nucleate from a full solid domain and converge to stable topologies with small influence on compliance. The designs produced by the proposed algorithm can successfully and reliably meet the multiple predefined constraints in various aerodynamics conditions.

We emphasize that a truly practical airfoil should perform well over a range of operating conditions, e.g. not just at a single angle of attack. In the present study we explored different aerodynamic conditions with different angle of attack to demonstrate the flexibility and effectiveness of our buckling constrained topology framework. If the real flight-frequency weight data can be acquired in the future for a specific flight, the optimization sensitivity at each angle of attack should be weighted and combined for the topology update. All numerical examples are configured in the low subsonic regime with free stream Mach numbers below ≈ 0.3. Accordingly, we solve the incompressible RANS equations and do not apply compressibility corrections. For applications where compressibility becomes important, the incompressible module can be replaced by a compressible RANS model with no change to the optimization loop or the discrete adjoint sensitivity computation.

Fig. 18 demonstrates how the optimized cross-section can be assembled into a practical aircraft wing segment: each rib-and-spar module fits seamlessly into the skin, supporting rapid fabrication (e.g., laser cutting, or additive manufacturing) and straightforward mechanical joining. The results from our method not only achieve improved structural performance but also produce designs ready for real-world implementation.

6. Conclusion

This work is the first airfoil topology optimization study considering both stiffness and stability criteria. This study contributes to the aircraft wing structure optimization field by including aerodynamic loadings. A turbulent RANS-ALE FSI analysis provides the pre-stressed state for a geometrically nonlinear buckling constraint. This coupled flow-structure-buckling workflow, implemented with a TOBS-GT pipeline, enables internal structural layouts that are not only stiff and lightweight but also stable under aerodynamic loading.

The stability of the airfoil is successfully improved regarding the buckling factor when compared to the compliance design. Augmented-Lagrangian multipliers are developed and a KS-aggregation strategy is used to avoid mode switching and improve the optimization stability. The algorithm is proven to be effective without the need of fine tuning optimization parameters in various cases including different speeds, angles of attack and FSI boundary condition setups. Significant stability enhancements are found in all numerical cases while little influences on stiffness are observed.

A significant advantage of the binary method is the non-existence of pseudo-buckling modes and erroneous load factors, which are inherently associated with intermediate density elements when applying density-based optimization. Besides, in a decoupled scheme, the optimizer produces design on a fixed optimization grid while the FSI and buckling physics are handled by external solvers. This separation proves convenient for multi-physics simulations and reduces the overall element count compared to meshing on the optimization grid, thereby reducing computational cost.

To capture large structural deformations, the fluid equations are solved in an Eulerian frame and the solid in a Lagrangian frame, which enables tracking the deformed FSI interface. Both the FSI and buckling analyses include geometric nonlinearities, and the implementation of a RANS turbulence model adds realism for complex aerodynamic load conditions. Nevertheless, the wing-like example is used to develop the workflow rather than to propose a real industrial design. The present framework does not yet include certification level load conditions, aeroelastic flutter, fatigue checks, or manufacturability rules. Industrial applications will also require assessing Brazier-induced crushing load in addition to the FSI loads considered here. Future work could focus on integrating real flight-data statistics for multiple angles of attack weighting, and extending the simulation to higher Reynolds number regimes, including transonic and supersonic flows.

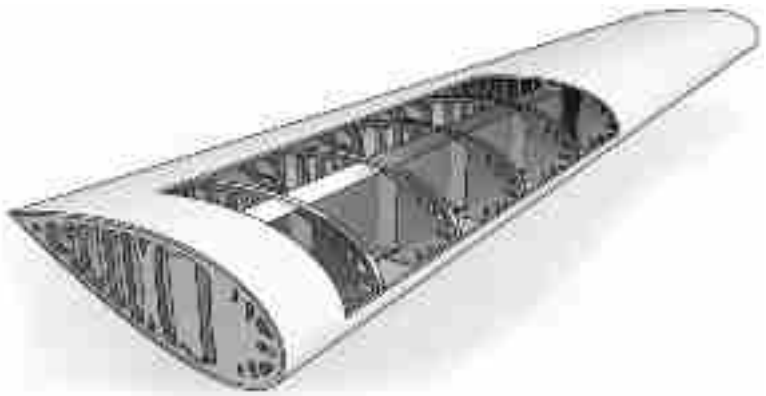

Fig. 18. Conceptual assembly of the NACA 0030 wing segment: topology optimized internal ribs and spars (dark gray) fitted within a continuous outer skin (light gray). The repeating cross-sectional modules can be rapidly fabricated via laser cutting and bolted together to form a full wing, illustrating the method's fabrication-friendly nature.

Data availability

More information on the data supporting the results of this work is available from the corresponding author upon reasonable request.

CRediT authorship contribution statement

Qingdi Wang: Writing – original draft, Visualization, Validation, Methodology, Investigation, Formal analysis, Data curation, Conceptualization. **Lucas Oliveira Siqueira:** Writing – review & editing, Methodology. **Tao Xu:** Writing – review & editing, Methodology. **Guanzhe Cui:** Writing – review & editing, Methodology. **Zhi Li:** Writing – review & editing, Visualization. **Anderson Soares da Costa Azevêdo:** Writing – review & editing. **Renato Picelli:** Writing – review & editing, Software, Funding acquisition. **Yi Min Xie:** Writing – review & editing, Supervision, Project administration, Funding acquisition, Conceptualization.

Declaration of competing interest

The authors confirm that they do not have any competing financial interests or personal relationships that could be perceived to influence the work presented in this paper.

Acknowledgment

The authors gratefully acknowledge the financial support from the Australian Research Council (FL190100014) and Sao Paulo Research Foundation (2021/05930–2).

Appendix A

This appendix presents the finite difference analysis used to verify the design sensitivities obtained via semi-automatic differentiation. We verify the adjoint sensitivities on a rectangular channel plate benchmark shown in Fig. A.1, where a structured solid mesh allows pointwise finite difference checks on the same grid, enabling a direct comparison. Air flow enters the channel from the left with a uniform inlet velocity corresponding to $Re = 1 \times 10^4$. At the outlet on the right a pressure condition $p = 0$ is imposed, and no slip conditions are applied on the top and bottom channel walls. The compliant plate (structural design domain) is clamped along its bottom edge. The fluid density is 1.225kg/m^3 and dynamic viscosity is 1.8×10^{-5} Pa·s. The solid is modeled in plane stress with Young's modulus $E = 10$ MPa and Poisson's ratio $\nu = 0.35$. The structural rectangle has a width of 1.4 m and height of 0.5 m and starts at x = 0.3 m. The optimization grid uses 140 elements in the x direction and 50 elements in the y direction.

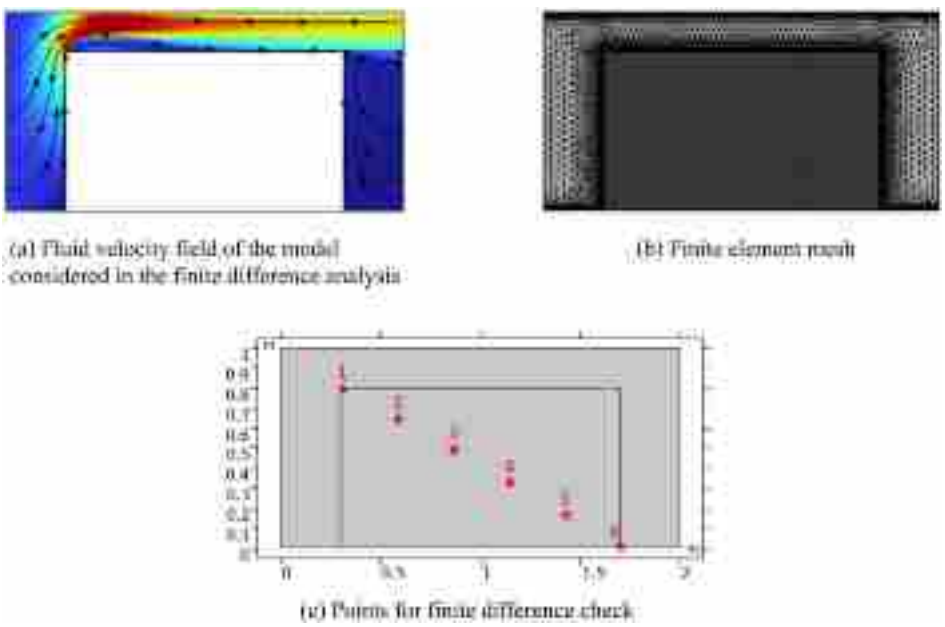

Fig. A.1. Gradient check setup for the finite-difference verification. (a) Velocity magnitude and streamlines of the RANS k-ε FSI solution; (b) finite element mesh; (c) locations used to compute central finite difference sensitivities.

Fig. A.1a and Fig. A.1b illustrate representative velocity fields and finite element mesh for this model. The sensitivities described in Eq. (35) are evaluated by the semi-automatic (discrete-adjoint) module. These values are checked by finite differences at a set of probe

points within the solid domain (Fig. A.1c). For the finite difference analysis, a central difference with a step size 1×10^{-4} is employed. Table A.1 reports the sensitivity values obtained via semi-automatic differentiation and via finite differences at the considered points. The maximum relative difference between the two methods does not exceed 0.01 %, which is small and validates the accuracy of the semi-automatic differentiation tool employed in this work.

(Table A1)

Table A.1
Compliance sensitivity results checked from finite difference analysis; SAD = semi-automatic differentiated sensitivities.

Point	Coordinates (x,y)	SAD [10^{-11} Nm]	FD [1]	Relative Difference (%)
1	(0.305,0.795)	-0.21660	-0.21660	0.000009
2	(0.585,0.645)	-0.83835	-0.83835	0.000705
3	(0.865,0.485)	-0.36495	-0.36494	0.000541
4	(1.145,0.325)	-0.29255	-0.29252	0.00789
5	(1.425,0.165)	-0.27177	-0.27175	0.00559
6	(1.695,0.005)	-3.5983	-3.5982	0.00209

References

[1] M.H. Sadraey, Structural Design, Springer, Cham, 2025, pp. 69–77, https://doi.org/10.1007/978-3-031-67795-3_5.
[2] M. Elelwi, R.M. Botez, T.-M. Dao, R. Pecora, I. Dimino, S. Ameduri, Structural sizing and topology optimization based on weight minimization of a variable tapered span-morphing wing for aerodynamic performance improvements, Biomimetics 6 (2021) 55, https://doi.org/10.3390/biomimetics6040055.
[3] V.O. Balabanov, R.T. Haftka, Topology optimization of transport wing internal structure, J. Aircraft 33 (1996) 232–233, https://doi.org/10.2514/3.46926.
[4] H.P. Buckley, B.Y. Zhou, D.W. Zingg, Airfoil optimization using practical aerodynamic design requirements, AIAA J 47 (2010) 1707–1719, https://doi.org/10.2514/1.C000256.
[5] S. Vasista, L. Tong, Topology-optimized design and testing of a pressure-driven morphing-aerofoil trailing-edge structure, AIAA J. 51 (2013) 1898–1907, https://doi.org/10.2514/1.J052239.
[6] J.S. Choi, L. Zhao, G.J. Park, S.K. Agrawal, R.M. Kolonay, Enhancement of a flapping wing using path and dynamic topology optimization, AIAA J. 49 (2011) 2616–2626, https://doi.org/10.2514/1.J050834.
[7] H. Namgoong, W.A. Crossley, A.S. Lyrintzis, Aerodynamic optimization of a morphing airfoil using energy as an objective, AIAA J. 45 (2007) 2113–2124, https://doi.org/10.2514/1.24355.
[8] J.D. Hodson, A.P. Christopherson, J.D. Deaton, A.M. Pankonien, G.W. Reich, P.S. Beran, Aeroelastic topology optimization of a morphing airfoil in supersonic flow using evolutionary design, AIAA Pap. 2019-1466 (2019), https://doi.org/10.2514/6.2019-1466.
[9] I. Gibert Martínez, F. Afonso, S. Rodrigues, F. Lau, R. Loja, A sequential approach for aerodynamic shape optimization with topology optimization of airfoils, Math. Comput. Appl. 26 (2021) 55, https://doi.org/10.3390/mca26050055 [paper].
[10] N. Ban, W. Yamazaki, Black-box function aerodynamic topology optimization algorithm via machine-learning technologies, AIAA J. 59 (2021) 5174–5185, https://doi.org/10.2514/1.J059605.
[11] F. Deng, C. Xue, N. Qin, Parameterizing airfoil shape using aerodynamic performance parameters, AIAA J. 60 (2022) 4399–4412, https://doi.org/10.2514/1.J061464.
[12] N. Nimura, A. Oyama, Multiobjective aerodynamic topology optimization using quadtree genetic programming, AIAA Pap. 2023-3473 (2023), https://doi.org/10.2514/6.2023-3473.
[13] K. Hirose, K. Suzuki, W. Yamazaki, Efficient aerodynamic topology optimization for supersonic airfoil using dimensionality-reduction methods, AIAA Pap. 2024-1406 (2024), https://doi.org/10.2514/6.2024-1406.
[14] K. Hirose, K. Suzuki, W. Yamazaki, Aerodynamic topology optimization of supersonic airfoils using feature extraction via dimensionality-reduction methods, in: Proc. Informit, 2024 T2025031300025491610211575, https://doi.org/10.3316/informit.t2025031300025491610211575 [paper].
[15] H. Li, T. Kondoh, P. Jolivet, N. Nakayama, K. Furuta, H. Zhang, B. Zhu, K. Izui, S. Nishiwaki, Topology optimization for lift–drag problems incorporated with distributed unstructured mesh adaptation, Struct. Multidiscip. Optim. 65 (2022) 14, https://doi.org/10.1007/s00158-022-03314-w [paper].
[16] L. Krog, A. Tucked, M. Kemp, R. Boyd, Topology optimization of aircraft wing-box ribs, in: Proc. 10th AIAA/ISSMO Multidisciplinary Analysis and Optimization Conf, Albany, NY, 2004, https://doi.org/10.2514/6.2004-4481. AIAA-2004-4481.
[17] T. Proença, F. Afonso, F. Lau, H. Policarpo, J. Lourenço, On the design and manufacturing of topologically optimized wings, Rapid Prototyp. J. 28 (2022) 637–646, https://doi.org/10.1108/RPJ-04-2021-0095.
[18] D. Walker, D. Liu, Topology optimization of an aircraft wing, in: Proc. 56th AIAA/ASCE/AHS/ASC Structures, Structural Dynamics, and Materials Conf, Kissimmee, FL, 2015, https://doi.org/10.2514/6.2015-0976. AIAA 2015-0976.
[19] N. Aage, E. Andreassen, B.S. Lazarov, O. Sigmund, Giga-voxel computational morphogenesis for structural design, Nature 550 (2017) 84–86, https://doi.org/10.1038/nature23911.
[20] P. Gomes, R. Palacios, Aerodynamic-driven topology optimization of compliant airfoils, Struct. Multidiscip. Optim. 62 (2020) 2117–2130, https://doi.org/10.1007/s00158-020-02600-9.
[21] K. Kambayashi, N. Kogiso, Fundamental study on aerodynamic-driven topology optimization of compliant morphing airfoil using panel method, in: Asia-Pacific Int. Symp. Aerospace Technol., Singapore, 2023, Lecture Notes in Electr. Eng 1051, Springer, Cham, 2024, pp. 1821–1829, https://doi.org/10.1007/978-981-97-4010-9_140.
[22] J. Syed, M. Ali, W. Muhammad, H.W. Embong, A. Aabid, Effect of cut-out shape on the stresses in aircraft wing ribs under aerodynamic load, CFD Lett 13 (2021) 87–94, https://doi.org/10.37934/cfdl.13.11.8794.
[23] J.H. Zhu, W.H. Zhang, L. Xia, Topology optimization in aircraft and aerospace structures design, Arch. Comput. Methods Eng. 23 (2015) 595–622, https://doi.org/10.1007/s11831-015-9151-2.
[24] B. Li, G.J. Kennedy, Buckling mode constraints for topology optimization using eigenvector aggregates, Comput. Methods Appl. Mech. Eng. 429 (2024) 117145, https://doi.org/10.1016/j.cma.2024.117145.
[25] Z.M. Malikov, M.E. Madaliev, S.L. Chernyshev, A.A. Ionov, Validation of a two-fluid turbulence model in COMSOL Multiphysics for the problem of flow around aerodynamic profiles, Sci. Rep. 14 (2024) 1–23, https://doi.org/10.1038/s41598-024-52673-5.
[26] P. Wriggers, Nonlinear Finite Element Methods, Springer, Berlin, 2008.
[27] E. Mendes, R. Sivapuram, R. Rodriguez, M. Sampaio, R. Picelli, Topology optimization for stability problems of submerged structures using the TOBS method, Comput. Struct. 259 (2022) 106685, https://doi.org/10.1016/j.compstruc.2021.106685.

[28] G. Kreisselmeier, R. Steinhauser, Systematic control design by optimizing a vector performance index. Computer Aided Design of Control Systems, Pergamon, Oxford, 1980, pp. 113–117, https://doi.org/10.1016/B978-0-08-024488-4.50022-X.
[29] T. Xu, X. Huang, X. Lin, Y.M. Xie, Topology optimization for maximizing buckling strength using a linear material model, Comput. Methods Appl. Mech. Eng. 417 (2023) 116437, https://doi.org/10.1016/j.cma.2023.116437.
[30] T.D. Tsai, C.C. Cheng, Structural design for desired eigenfrequencies and mode shapes using topology optimization, Struct. Multidiscip. Optim. 47 (2013) 673–686, https://doi.org/10.1007/s00158-012-0840-2.
[31] S. Townsend, H.A. Kim, A level set topology optimization method for the buckling of shell structures, Struct. Multidiscip. Optim. 60 (2019) 1783–1800, https://doi.org/10.1007/s00158-019-02374-9.
[32] T. Xu, X. Huang, X. Lin, Y.M. Xie, Topology optimization of continuum structures for buckling resistance using a floating projection method, Comput. Methods Appl. Mech. Eng. 429 (2024) 117204, https://doi.org/10.1016/j.cma.2024.117204.
[33] C.S. Andreasen, O. Sigmund, Topology optimization of a reversible crash protection using fluid–structure interaction, in: Proc. 10th AIAA/ISSMO Multidisciplinary Analysis and Optimization Conf, Albany, NY, 2004. AIAA 2004-4481.
[34] K.E.S. Silva, R. Sivapuram, S. Ranjbarzadeh, R.S. Gioria, E.C.N. Silva, R. Picelli, Topology optimization of stationary fluid–structure interaction problems including large displacements via the TOBS-GT method, Struct. Multidiscip. Optim. 65 (2022) 1–18, https://doi.org/10.1007/s00158-022-03442-3.
[35] L.O. Siqueira, R.L. Cortez, R. Sivapuram, S. Ranjbarzadeh, R.S. Gioria, E.C.N. Silva, R. Picelli, Topology optimization for stationary fluid–structure interaction problems with turbulent flow via sequential integer linear programming and smooth explicit boundaries, Adv. Eng. Softw. 190 (2024) 103599, https://doi.org/10.1016/j.advengsoft.2024.103599.
[36] C. Raspanti, J. Bandoni, L. Biegler, New strategies for flexibility analysis and design under uncertainty, Comput. Chem. Eng. 24 (2000) 2193–2209, https://doi.org/10.1016/S0098-1354(00)00591-3.
[37] G.J. Kennedy, J.E. Hicken, Improved constraint-aggregation methods, Comput. Methods Appl. Mech. Eng. 289 (2015) 332–354, https://doi.org/10.1016/j.cma.2015.02.017.
[38] R. Picelli, E. Moscatelli, P.V.M. Yamabe, D.H. Alonso, S. Ranjbarzadeh, R.S. Gioria, J.R. Meneghini, E.C.N. Silva, Topology optimization of turbulent fluid flow via the TOBS method and a geometry-trimming procedure, Struct. Multidiscip. Optim. 65 (2022) 34, https://doi.org/10.1007/s00158-021-03118-4.
[39] R. Picelli, R. Sivapuram, Y.M. Xie, A 101-line MATLAB code for topology optimization using binary variables and integer programming, Struct. Multidiscip. Optim. 63 (2021) 935–954, https://doi.org/10.1007/s00158-020-02719-9.
[40] X. Huang, Y. Xie, Convergent and mesh-independent solutions for the bi-directional evolutionary structural optimization method, Finite Elem. Anal. Des. 43 (2007) 1039–1049, https://doi.org/10.1016/j.finel.2007.06.006.
[41] T. Xu, X. Lin, Y.M. Xie, Bi-directional evolutionary structural optimization with buckling constraints, Struct. Multidiscip. Optim. 66 (2023) 1–15, https://doi.org/10.1007/s00158-023-03517-9.
[42] K. Kambayashi, N. Kogiso, Fundamental study on aerodynamic-driven topology optimization of compliant morphing airfoil using panel method, in: Asia-Pacific Int. Symp. Aerospace Technol., Singapore, 2023, Lecture Notes Electr. Eng 1051, Springer, Cham, 2024, pp. 1821–1829, https://doi.org/10.1007/978-981-97-4010-9_140.